ADVANCED FUNCTIONAL MATERIALS
www.afm-journal.de

Positive and Negative Pressure Regimes in Anisotropically Strained V_2O_3 Films

*Eti Barazani, Dip Das, Chubin Huang, Abhishek Rakshit, Cecile Saguy, Pavel Salev, Javier del Valle, Maytal Caspary Toroker, Ivan K. Schuller, and Yoav Kalcheim**

The metal-insulator phase transitions in V_2O_3 are considered archetypal manifestations of Mott physics. Despite decades of research, the effects of doping, pressure, and anisotropic strains on the transitions are still debated. To understand how these parameters control the transitions, anisotropically strained pure V_2O_3 films are explored with nearly the same contraction along the *c*-axis, but different degrees of ab-plane expansion. With small ab-plane expansion, the films behave similar to bulk V_2O_3 under hydrostatic pressure. However, with large ab-plane expansion, the films are driven into the "negative pressure" regime, similar to that of Cr-doped V_2O_3, exhibiting clear coexistence of paramagnetic insulator and paramagnetic metal phases between 180–500 K. This shows that *c*-axis contraction alone, or an increase in c/a ratio is insufficient for inducing "negative pressure" effects. Actually, *c*-axis contraction alone destabilizes the two insulating phases of V_2O_3, whereas *a*-axis expansion tends to stabilize them. The effects of strain are modeled using density functional theory providing good agreement with experimental results. The findings show that chemical pressure alone cannot account for the phase diagram of $(V_{1-x}Cr_x)_2O_3$. This work enables to manipulate a Mott transition above room temperature, thereby expanding the opportunities for applications of V_2O_3 in novel electronics.

1. Introduction

V_2O_3 is a paramagnetic metal (PM) at room temperature and undergoes a transition to a paramagnetic insulator (PI) with Cr doping. The PM-PI transition in $(V_{1-x}Cr_x)_2O_3$ is considered to be the archetypal Mott transition, involving no change in crystal symmetry or magnetic ordering.[1–3] Both PM and PI phases have rhombohedral corundum structure but with different lattice constants.[4,5] The PI phase is stabilized with Cr doping of $x > 0.005$ and $T > 185$ K (see **Figure 1**a) and a thermal PM-to-PI transition occurs at certain doping levels. Far above room temperature, Kuwamoto et al.[4] have argued that the PI phase evolves through a second order transition into a high temperature metallic phase that is similar to the PM phase of pure V_2O_3. In the low temperature regime, below 160–185 K, $(V_{1-x}Cr_x)_2O_3$ becomes an antiferromagnetic insulator (AFI) through a first order phase transition. The application of hydrostatic pressure has been shown to suppress both the PI and AFI phases, driving the system into the PM phase, thus counteracting the effect of Cr-doping. Ti doping exhibits similar phenomenology to hydrostatic pressure, which has led to the interpretation of Cr and Ti doping in the context of chemical pressure: Ti doping or positive pressure increase the bandwidth, thereby stabilizing the PM phase. Negative pressure, or Cr doping, reduce the bandwidth and therefore stabilizes both the PI and AFI phases. However, several works have contested this hypothesis arguing that Cr-doping drives the PM-to-PI transition through

E. Barazani, D. Das, C. Huang, A. Rakshit, M. C. Toroker, Y. Kalcheim
Materials Science and Engineering Department
Technion – Israel Institute of Technology
Haifa 3200003, Israel
E-mail: ykalcheim@technion.ac.il

The ORCID identification number(s) for the author(s) of this article can be found under https://doi.org/10.1002/adfm.202211801

DOI: 10.1002/adfm.202211801

C. Saguy
Solid State Institute
Technion – Israel Institute of Technology
Haifa 3200003, Israel

P. Salev
Department of Physics and Astronomy
University of Denver
Denver, CO 80208, USA

J. del Valle
Department of Physics
University of Oviedo
C/ Federico García Lorca 18, Oviedo 33007, Spain

I. K. Schuller
Department of Physics and Center for Advanced Nanoscience
University of California-San Diego
La Jolla, CA 92093, USA

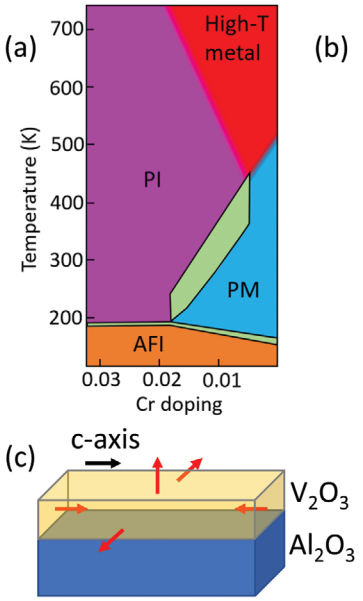

	T_C [K]	a [Å]	b [Å]	c [Å]	α [deg]	β [deg]	γ [deg]
Bulk V_2O_3	156 K	4.951	4.951	14.003	90	90	120
300 nm V_2O_3 on $(11\bar{2}0)$ Sapphire - **A1**	144 K	4.957 ±0.001 (+0.13%)	4.958 ±0.001 (+0.13%)	13.866 ±0.006 (-0.98%)	89.98 ±0.03 (-0.03%)	90.09 ±0.03 (+0.10%)	119.64 ±0.02 (-0.30%)
300 nm V_2O_3 on $(11\bar{2}0)$ Sapphire - **A2**	166 K	4.971 ±0.002 (+0.41%)	4.969 ±0.001 (+0.37%)	13.859 ±0.004 (-1.03%)	90.04 ±0.03 (+0.04%)	89.95 ±0.04 (-0.05%)	119.88 ±0.02 (-0.10%)
300 nm V_2O_3 on $(10\bar{1}0)$ Sapphire – **M**	178 K	4.977 ±0.001 (+0.52%)	4.973 ±0.001 (+0.45%)	13.870 ±0.004 (-0.95%)	90.00 ±0.03 (+0.00%)	90.03 ±0.02 (+0.03%)	119.95 ±0.01 (-0.04%)

Figure 1. Phase diagram of bulk $(V_{1-x}Cr_x)_2O_3$, and anisotropic strains in films of pure V_2O_3 grown on various sapphire substrates with different orientations. a) Canonical phase diagram of Cr-doped V_2O_3 showing the antiferromagnetic insulator (AFI), paramagnetic metal (PM) and paramagnetic insulator (PI) phases (based on ref).[4] Green regions bounded by solid lines denote regimes of phase coexistence due to first order transitions. Second order transitions are shown as gradual changes in color. b) Comparison of room-temperature lattice parameters of the paramagnetic metallic phase in 300 nm V_2O_3 films grown on $(11\bar{2}0)$ and $(10\bar{1}0)$ oriented sapphire substrates. T_C corresponds to the PM-AFI transition temperature, taken from resistance versus temperature curves (Figure 2). Values in parentheses represent the expansion relative to bulk values. The difference between samples A1 and A2 is in the surface morphology and miscut angle of the sapphire substrates. In all films, a similar compressive strain of nearly −1% is found in the *c*-axis along with varying degrees of expansion in the ab-plane. See Section S2 (Supporting Information), for error calculation. c) schematics of the contraction along the *c*-axis and the expansion of the ab-plane observed in all samples.

changes in the orbital occupancy whereas pressure has the effect of increasing bandwidth without affecting orbital occupancy.[5,6] Using density functional theory and dynamical mean field theory it was argued that Cr-doping results in lattice distortions that favor the PI phase, while Ti-doping suppresses the AFI phase by charge doping.[7,8] Understanding the effects of doping and stress have thus been the subject of intense research focused on understanding the mechanisms for the metal-insulator transitions (MIT) observed in this system, but a clear picture has not yet emerged. From an applications perspective, manipulating an MIT above room temperature, as found only in few other compounds, is especially important for novel memory elements and resistive/threshold switching devices.[9–11] To tackle these challenges we studied thin films of pure V_2O_3 that exhibit anisotropic tensile and compressive strains that are inaccessible in bulk samples, driving V_2O_3 into different regimes of its phase diagram. These findings elucidate the role of *a*- and *c*- axis strains, and the difference between doping and strain. The results are supported by phase stability analysis performed using density functional theory (DFT) calculations. This understanding paves the way toward applications based on a room temperature MIT in V_2O_3.

Recent works have shown that thins films of pure and doped V_2O_3 can exhibit much of the phenomenology found in the canonical phase diagram of V_2O_3. For instance, in several studies, thin films were driven into an insulating state by Cr-doping.[12–15] Moreover, it was demonstrated that by varying the Fe concentration in a $(Cr_{1-y}Fe_y)_2O_3/Cr_2O_3$ buffer layer grown on top of *c*-axis oriented sapphire (Al_2O_3) substrates, the *a*-axis of pure and Cr-doped V_2O_3 films could be varied substantially leading to an isothermal room-temperature transition between metallic and insulating states as a function of substrate-induced stress.[14] However, unlike Cr-doped V_2O_3 single crystals, the strained films showed insulating behavior in the entire temperature regime above the transition from the AFI phase, which was interpreted as stabilization of intermediate phases, or possibly to PM/PI phase coexistence at the nanoscale. Also, using tip-induced stress,[16] it was found that compressive stress along the *c*-axis bares similarity to the Cr-doping regime of the V_2O_3 phase diagram. Growth of V_2O_3 films on sapphire substrates cut along different crystallographic orientations has also shown to produce large variations in PM/AFI transition temperatures.[17–23] Recently, it was shown that in (0001)-oriented V_2O_3 films, the PM-AFI transition is subjected to self-induced strain due to geometric confinement of the film.[18] This causes large in-plane compressive stress and out-of-plane expansion by the Poisson effect. Consequently, the trajectory of the phase transition follows the phase equilibrium line between the AFI and PM phases down to absolute zero. Different strains have also been considered theoretically,[24] arguing for a non-trivial dependence of the PM-AFI transition temperature on strain anisotropy, due to changes in length of one of the V–V bonds along the monoclinic *b*-axis that has a large impact on magnetic energy. Despite the large amount of work, several issues remain unclear: 1) That structural distortions stabilize the different phases in pure V_2O_3? 2) Can substrate orientation and morphology be used to tune these distortions and

access the PM/PI phase coexistence regime? 3) Is the effect of Cr doping in V_2O_3 limited to the chemical strain that it applies?

In the present work we answer these questions by comparing films grown on sapphire substrates of $(11\bar{2}0)$ and $(10\bar{1}0)$ orientations. We report three main findings: 1) Surprisingly, even though all films exhibit compressive strain along the *c*-axis and tensile strain in the ab-plane, they manifest phenomenology ranging from positive to negative pressure regimes, as in the canonical V_2O_3 phase diagram.[2] *c*-axis contraction induces the PI phase only when it is accompanied by large expansion of the *a*/*b*-axis through the Poisson effect. Without an *a*/*b*-axis expansion, the *c*-axis contraction drives V_2O_3 into the positive pressure regime. 2) The magnitude of *a*/*b*-axis expansion, and thus electrical transport properties of the film, depends strongly on the details of the substrate surface as well as its crystallographic orientation. 3) The ab-plane expansion required to induce effects similar to Cr-doping is much larger than that observed in bulk $(V_{1-x}Cr_x)_2O_3$, showing that Cr-induced chemical pressure alone cannot account for the phenomenology observed in the phase diagram.

2. Results and Discussion

To study the effects of anisotropic stress, V_2O_3 films of 300 nm thickness were grown using RF magnetron sputtering at a substrate temperature of 700 °C. A quenching process was performed immediately after growth to obtain high quality films.[25] Films were grown simultaneously on sapphire substrates cut along the a-plane $(11\bar{2}0)$ (samples A1 and A2) and m-plane $(10\bar{1}0)$ (sample M) to ensure similar growth conditions. Previous work from our group has shown that these V_2O_3 films grow epitaxially following the crystallographic orientation of the substrates.[25,26] The substrates used for growing samples A1 and A2 showed different miscut angles and roughness, as measured by AFM (see Section S1, Supporting Information). To measure lattice constants in films with growth orientations where the rhombohedral symmetry may be broken (as in the present case), for each film over 13 Bragg peaks were measured by x-ray diffractometry and lattice parameters were refined using a least mean squares method with no restriction on lattice symmetry (see Section S2, Supporting Information, for details).

As shown in Figure 1b, all films exhibit compressive strain along the [0001] orientation (*c*-axis) and tensile strain in the ab-plane. This is inconsistent with lattice constant mismatch strain since the unit cell of sapphire is 4–7% smaller than that of V_2O_3 and relaxes within a few nanometers from the interface with the substrate during the high-temperature growth.[27,28] Rather, the observed trend is consistent with the thermal expansion mismatch between sapphire and V_2O_3.[19,29–31] As the sample is cooled from the deposition temperature, the thermal expansion mismatch between the substrate and the film results in strain that may not relax even for large film thickness (300 nm in the present work). A comparison of reported lattice parameters of Al_2O_3 and V_2O_3 at the growth temperature (700 C) versus room temperature yields a −0.9% compressive strain for the *c*-axis and +0.74% tensile strain in the ab-plane, consistent with the type of distortion we observe. Despite the similar contraction of the *c*-axis, the different films show varying degrees of *a*/*b*-axis tensile strains—by nearly a factor of 4. This difference may be related to varying film density as recently reported in ref.[18] There, it was found that $V_2O_3(11\bar{2}0)$ films grown on substrates as those used for the growth of sample A1 have a density of 100% (to measurement accuracy) that would hinder the ab-plane expansion entailed in the PM-to-PI transition. On the other hand, the density is considerably lower in $V_2O_3(10\bar{1}0)$ films (as in sample M), permitting a larger expansion. The exact mechanism resulting in the different ab-plane expansion in the different films is a subject of current investigation (see Sections S1 and S2, Supporting Information, for details).

Since in bulk Cr-doped V_2O_3 the PI phase has a contracted *c*-axis and expanded *a*-axis compared to the PM phase, compressive strain along the *c*-axis (or a decrease in the c/a ratio) has been argued to drive the system toward the "negative" pressure regime of the V_2O_3 phase diagram.[5,16,32] It is therefore expected that in all the samples studied here the AFI-PM transition temperature would increase, albeit to different extents. However, as deduced from resistance versus temperature (RT) measurements (**Figure 2**), the film with the smallest in-plane expansion (A1) has a lower transition temperature (144 K) compared to bulk V_2O_3 (156 K), similar to the effect of positive pressure. In samples A2 and M, which have larger *a*/*b*-axis expansion (on average 0.39% and 0.49% respectively), the PM-AFI transition temperature rises and exceeds the bulk value (166 K for A2 and 178 K for M), similar to the effect of Cr-doping or negative pressure. Both samples also show anomalous resistance above 200 K. For sample M the RT curve shows signatures of a partial first order PM-PI phase transition, as demonstrated by additional hysteresis loops at 200–500 K. Also, the slope of the RT curve for sample M is about six times larger in this temperature range compared to sample A1 (red curve), signifying that the change in resistivity is due to an MIT rather than the temperature dependence of resistivity of the PM phase. In sample A2 the ab-plane expansion is smaller than in sample M, and only a resistance anomaly is observed, indicating proximity to the PM-PI transition (purple arrow in Figure 2b), as observed in pure and lightly doped V_2O_3 even without formation of the PI phase.[4] The differences between samples A1 and A2 are especially striking since the films are grown on substrates cut along the same crystallographic plane. The miscut angle of both substrates, however, varies by a factor of 8 (0.08° for sample A1 and 0.01°, see Section S1, Supporting Information). The mechanism behind the different ab-plane expansion in both cases is a subject of current research. One possibility is that it is related to different film densities that allow for different degrees of *a*/*b*-axis expansion (see section S1, Supporting Information). Regardless of the exact mechanism, these findings show that *c*-axis contraction induces a PM-to-PI transition only when accompanied by an *a*/*b*-axis expansion due to the Poisson effect. Otherwise, it destabilizes both the PI and AFI phases, similar to the effect of positive pressure.

We note that an increase in V:O ratio is known to increase the PM-AFI transition temperature, similar to the observed trend in our films. However, since our films are grown simultaneously, V:O ratio variations between samples are not to be expected. Indeed, we have performed time-of-flight secondary ion mass spectroscopy on our films (see section S3, Supporting Information) and found that V:O ratios in our samples are nearly the same within the measurement error. Moreover, V:O ratio variations are not known to induce a transition into the PI phase, as found in

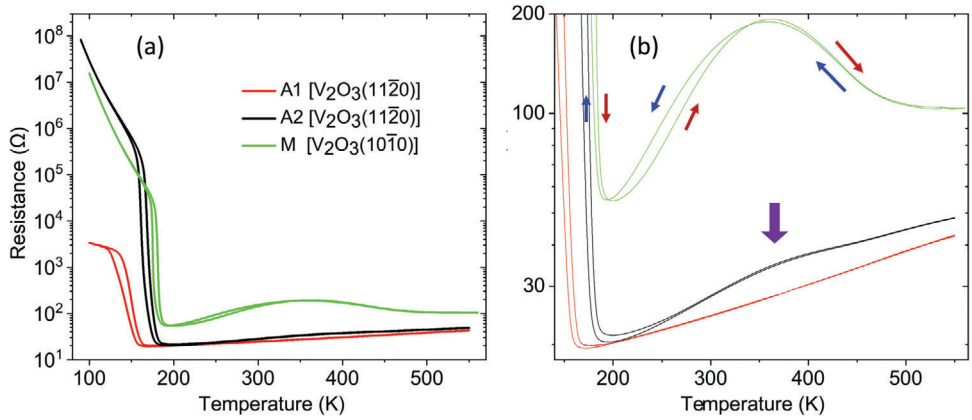

Figure 2. Resistance versus temperature of 300 nm V_2O_3 films. a) Full resistance versus temperature curve measured first by cooling and then by heating. The AFI-PM transition temperature of sample A1 ≈144 K (red) is considerably lower than the bulk value (156 K) and shows only one hysteresis loop at the AFI/PM transition. In contrast, sample A2 (black) and M (green) have higher transition temperatures than bulk V_2O_3 (166 and 178 K, respectively), indicating that these samples are in the "negative" pressure regime. b) Zoom-in of the high temperature portion of the RT curves. Sample A2 shows a resistance anomaly around 375 K (purple arrow), indicative of proximity to the PI phase.[4] Sample M shows three hysteresis loops: the first, centered around 178 K corresponds to the transition from pure AFI to the PM/PI coexistence regime. The second and third loops observed in sample M (between 200–340 K and above 340 K) correspond to a partial PM-PI transition and then a transition into a fully metallic phase with dR/dT → 0 above ≈500 K. The hysteresis loops show the first order nature of all transitions. Arrows indicate the resistance branches corresponding to cooling and heating cycles. See Section S7 (Supporting Information) for a discussion of the resistive transition in sample A1.

sample M and have a negligible effect on strain (<0.1%), which is inconsistent with the large strains found in our samples.[33]

To investigate the origin of the resistance anomalies in the "negative pressure" regime, we focus on sample M that shows the largest anomaly, and correlate its transport properties with the structural properties as measured by variable temperature X-ray diffractometry (XRD) (**Figure 3**). Reciprocal space maps (RSMs) show that at low temperature only a single Bragg peak is found corresponding to the AFI phase. Once this peak disappears upon heating, two different structural peaks appear. This is in contrast with the (11$\bar{2}$0) growth orientation that exhibits only one structural peak above the AFI-PM transition temperature as is the case for similarly grown V_2O_3(10$\bar{1}$2) and V_2O_3(0001) films.[18,26] Since sample M has low resistance above 200 K (comparable to that of samples A1 and A2), we attribute the dominant peak (at larger Q-vectors) to the PM phase. Since the sample shows "negative pressure" effects we attribute the second peak to the PI phase. This is also consistent with larger a/b lattice parameters expected from the PI phase relative to the PM phase. As temperature increases, intensity shifts from the PM peak to the PI peak (**Figure 4**a), consistent with the canonical phase diagram of V_2O_3 where increasing temperature in the "negative" pressure regime leads to a transition from AFI to PM and then to PI (see Figure 1a in Cr-doping regime of $0.005 < x < 0.018$). According to the canonical phase diagram, a full transition to the PI phase should occur as temperature

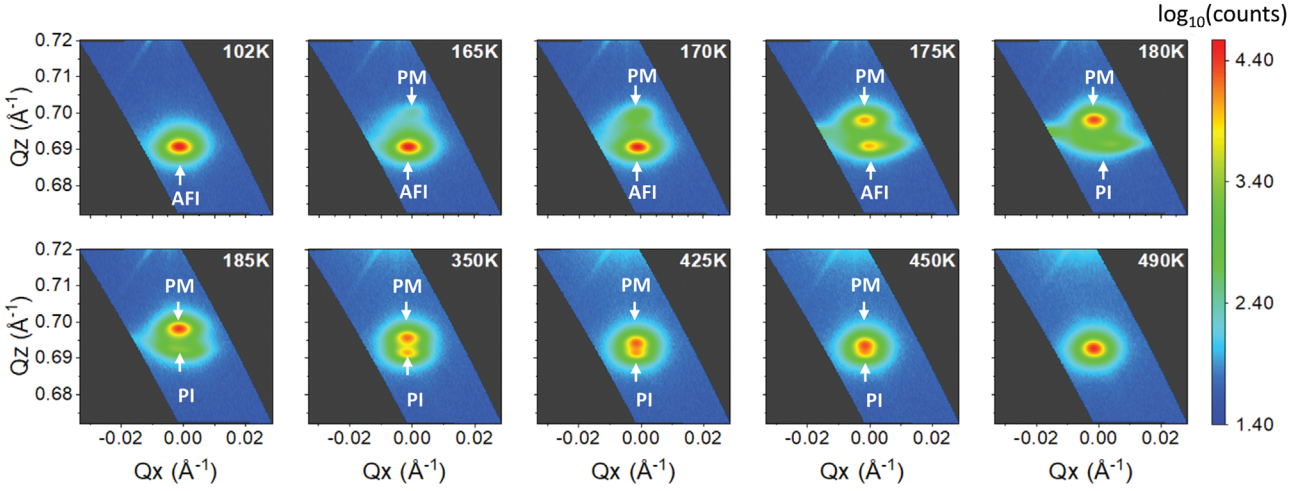

Figure 3. Evolution of the structural transitions of a 300 nm thick V_2O_3(10$\bar{1}$0) film (sample M) as a function of temperature. Reciprocal space maps measured by X-ray diffractometry in the vicinity of the rhombohedral PM (30$\bar{3}$0) peak show that as the Bragg peak associated with the AFI disappears at 185 K, two Bragg peaks associated with the PM and PI phases appear immediately. With increasing temperature, the Bragg peaks tend to merge and their intensities change non-monotonously—see Figure 4 for analysis.

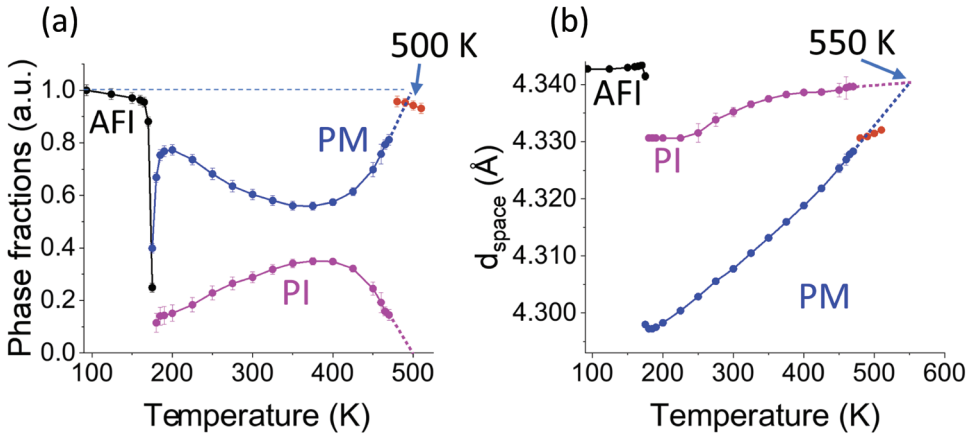

Figure 4. Temperature dependence of structural phase fractions a) and d-spacings b) for the AFI, PM, and PI phases corresponding to the Bragg peaks shown in Figure 3. The PM and PI phases appear immediately with the disappearance of the AFI phase. With increasing temperature, the PI phase fraction increases at the expense of the PM phase until 380 K where the trend reverses. This differs from the canonical V_2O_3 phase diagram in which the PI phase is expected to become more dominant at these temperatures. With increasing temperature the d-spacings of the PM and PI converge due to different thermal expansion coefficients, merging at 550 K. Extrapolation of phase fractions in (a) shows that for sample M the PM phase fraction already reaches 100% at a lower temperature of 500 K. Due to the large overlap between the two Bragg peaks, above 470 K reciprocal space maps are fitted to a single peak (red dots). Where error bars are not shown they are smaller than the size of the dot.

increases. Surprisingly, however, > 370 K, the intensity of the Bragg peak associated with the PM phase starts increasing at the expense of that of the PI phase. This is consistent with the downturn in resistance at about the same temperature. Extrapolation of phase fractions shows that the two phases coexist until ≈500 K (Figure 4) at which point the PM phase reaches 100% and the PI phase disappears completely. It is worth noting that the PI phase fraction does not exceed 35% at any temperature, which is too low to disrupt percolation of metallic regions, explaining the low resistance observed at all temperatures above 185 K. With increasing temperature, the d-spacing of the PM and PI peaks grow closer due to the different thermal expansions of the two phases. By extrapolation, they become identical at 550 K, providing an upper limit for the critical point that would terminate the first order phase transition line. Above 520 K the slope of the RT curve tends to zero indicating that the sample is no longer insulating and fully driven into the high-T metal phase.

If the structural phase coexistence observed by XRD >200 K is indeed related to the PM/PI phase coexistence as suggested, it is expected that the local conductivity would vary significantly as observed in other material systems.[34–37] To test this, we measured conductive atomic force microscopy maps, which revealed large variations in current-voltage characteristics, attributed to PI and PM domains (see **Figure 5**). The maps reveal that PM/PI domains are elongated in the direction of the *c*-axis with a typical width of ≈100 nm. While they bear similarity in size and directionality to topographic features, no direct correlation between grain structure and PI/PM domains is observed, where in many cases similar topographic features can show either high or low local conductivity. This corroborates the XRD data, showing PM/PI phase coexistence at temperatures >200 K, including room temperature.

Taken together, these findings call for an addition to the phase diagram of V_2O_3 for the case of anisotropic strain with similarities and differences with respect to Cr-doping (see **Figure 6**). For bulk $(V_{1-x}Cr_x)_2O_3$ in the range $0.005 < x < 0.018$ it was shown that three transitions occur: AFI → PM → PI → high-T metal.[4] In sample M, similar phase transitions are observed but with three

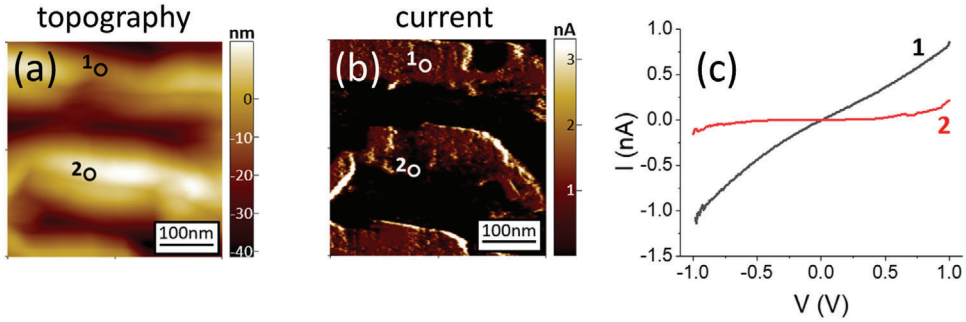

Figure 5. Coexistence between regions of high and low conductivity in sample M ($V_2O_3(10\bar{1}0)$ film) as measured by room-temperature conductive atomic force microscopy. Topography and current images are shown in (a) and (b), respectively with two representative points in which IV measurements were taken showing conducting and insulating behavior (c). See Section S5 (Supporting Information) for measurement details.

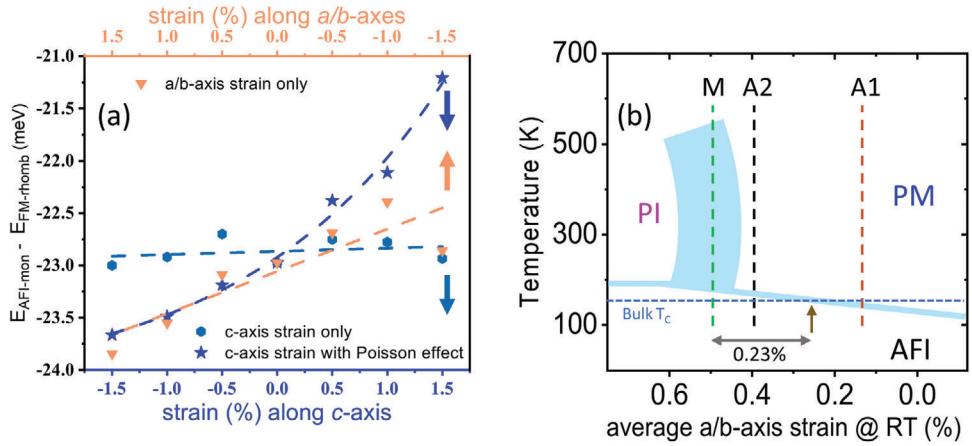

Figure 6. Effect of different strain configurations on the stability of the phases of V_2O_3. a) DFT calculation of the total energy difference between monoclinic AFI and rhombohedral FM states of V_2O_3 under various strain configurations w.r.t the rhombohedral axes, as indicated (note the different *x*-axes for *c*-axis and *a*/*b*-axes strain). *c*-axis strain is insufficient for increasing the stability regime of the AFI phase (turquoise) that occurs only with expansion of the *a*/*b*-axis, either purely (orange) or due to the Poisson effect (blue). b) suggested addition to the V_2O_3 phase diagram for the case of anisotropic strain—with −1% contraction of the *c*-axis, based on the experimental results. Blue shaded regions denote phase coexistence regions. The vertical dashed lines correspond to the thermally observed transitions in the A1, A2, and M samples each having a different average ab-plane expansion. The PM-PI coexistence regime is broadened and curved, resulting in a non-monotonous temperature dependence of PM-PI phase fractions for sample M. The termination of the first order PM/PI coexistence regime is at 550 K, as deduced by convergence of the PM and PI lattice structures due to differences in thermal expansion of the two phases (see Figures 3 and 4b). The PM/AFI transition temperature in bulk V_2O_3 is denoted by a horizontal line. This temperature is attained with *c*-axis strain of −1% and *a*-axis strain of 0.25% as denoted by the brown arrow.

main differences. The first difference is that there is no simple equivalence between Cr doping and anisotropic strain. Namely, the AFI phase in $V_2O_3(10\bar{1}0)$ vanishes at 185 K that would correspond to a doping of x = 0.014 in bulk $(V_{1-x}Cr_x)_2O_3$. However, for this doping level the transition to the high temperature metallic phase occurs at T > 650 K[4] whereas the onset of the high T metallic state in the M sample is already at ≈380 K. The second difference is that the PM/PI phase coexistence regime occurs over <80 K in $(V_{1-x}Cr_x)_2O_3$ for any doping level whereas in sample M it is observed within a range of 300 K. The third difference is that the transition to the high-T metal phase is hysteretic revealing its first order nature (see Section S6, Supporting Information). A possible explanation for these differences is that strain results in a smaller free energy difference between the PM and PI phases as compared to Cr doping. Thus, the PM-to-PI transition is more gradual than in the Cr-doped case. At higher temperatures where the structures of the two phases tend to merge, the PM is again favored so that the transition into the PI is never fully complete.

A comparison between the strains in the films studied here and the strain caused by Cr doping in bulk V_2O_3, shows that in the latter case, strain cannot account for the increase in PM-AFI transition temperature and stabilization of the PI phase. Namely, Cr doping of 1% induces an expansion of 0.04% in the *a*-axis and a contraction of <0.01% in the *c*-axis.[38] At this Cr concentration the PM-AFI transition temperature increases by ≈20 K and the PI phase is completely stabilized above 360 K (see Figure 1a). The present findings show that in pure (and ansiotropically strained) V_2O_3 a similar increase in PM-AFI transition temperature is only obtained by increasing the *a*/*b*-axis tensile strain by 0.23%, nearly six times larger than the 0.04% increase observed in 1% Cr doped V_2O_3 (see Figure 6). Moreover, despite the large expansion, the PI phase is not fully stabilized at any temperature. This indicates that the expansion of the *a*-axis due to Cr doping is not the main driving mechanism of the phenomenology observed in $(V_{1-x}Cr_x)_2O_3$. These findings are consistent with recent theoretical studies suggesting that Cr doping induces orbital polarization and local distortions that stabilize the PI phase.[8,24] These local effects drive Cr-doped V_2O_3 into the PI phase with little overall strain. This explains also previous X-ray absorption measurements showing differences in bandwidth and orbital occupation between the PM phases of pure V_2O_3 and pressurized Cr-doped V_2O_3.[5,6]

To gain a deeper understanding of the effect of anisotropic strain in determining whether V_2O_3 is driven into the positive or negative pressure regimes we calculated the energies of the AFI and PM phases as a function of strain using DFT, based on previous work by Wickramaratne et al.[24] Since only magnetically ordered or non-magnetic phases can be modeled in DFT we used ferromagnetic coupling in the rhombohedral phase as a proxy for the PM phase.[39,40] We calculated the variation in energy of both ferromagnetic metal (FM) and AFI phases with anisotropic strains in the same crystallographic orientations with respect to the rhombohedral unit cell of the FM: 1) Equibiaxial strain along a/b with fixed *c*-axis. 2)Uniaxial strain along the *c*-axis with fixed *a*/*b*-axes. 3) *c*-axis strain along with equibiaxial strain in the *a*/*b*-axes according to the Poisson effect (see Section S8, Supporting Information, for details). In Figure 6a, we plot the difference in energy between the two phases $\Delta E = E_{AFI} - E_{FM}$ as a function of the various strains. A decrease in ΔE indicates stabilization (destabilization) of the AFI (FM) phase and therefore an increase (decrease) in FM-AFI transition temperature. As expected, tensile strain in the ab-plane (orange) increases the FM-AFI transition temperature, thereby driving V_2O_3 into the negative pressure regime. However, *c*-axis strain alone (with no concomitant *a*/*b*-axis strain) is found to have a negligible effect on the stability

of either phase (turquoise). Only when the c and ab-plane strain are included according to the Poisson effect (blue), the stability of both phases follows the expected trend of driving V_2O_3 into the negative pressure regime with compression along the *c*-axis (and ab-plane expansion). These results corroborate our findings that *c*-axis compressive strain alone is insufficient for inducing negative pressure effects but rather that the a/b-plane expansion that ensues due to the Poisson effect plays the dominant role.

3. Conclusion

In conclusion, this works tackles three issues regarding the canonical Mott insulator V_2O_3. Using thin films exhibiting different anisotropic strains, we show that when strain predominantly constitutes of a *c*-axis contraction, the PM-AFI transition temperature is reduced and the PI phase can be completely destabilized, similar to the effect of positive hydrostatic pressure. However, if the *c*-axis contraction entails a large ab-plane expansion, the PM-AFI transition temperature increases and the PI phase is induced, as in the "negative" pressure regime of the V_2O_3 phase diagram. A comparison between the distortions observed in films of the present study with those of Cr-doped bulk samples shows that the simplistic chemical pressure scenario cannot account solely for the phase diagram of $(V_{1-x}Cr_x)_2O_3$. Our results also show that opposite pressure regimes of the V_2O_3 phase diagram can be accessed in thin films by growth on substrates with different orientations, roughness, and miscut angle. These findings provide a guide to judiciously manipulate strain and doping to affect the most important degrees of freedom dominating the phase transitions in V_2O_3. The ability to achieve a PM-PI phase transition in V_2O_3 thin films above room temperature is a major step toward functionalizing this canonical Mott transition for applications in novel electronics.

Statistical Analysis

Several samples were grown in similar conditions to A1, A2, and M showing similar characteristics. Errors in lattice parameters due to the uncertainty in 2θ were estimated by performing structural refinement with 100 sets of 2θ values for all Bragg peaks where each 2θ was randomly selected in the range $\pm$ 0.01° of the measured value. The total error shown in the main text (Figure 1b) is the variance of the 100 structural refinements of the six lattice parameters. See Section S2 (Supporting Information), for details.

Supporting Information

Supporting Information is available from the Wiley Online Library or from the author.

Acknowledgements

The work at the Technion was supported by the Israel Science Foundation grant no. 1031/21 and the European Research Council. This project has received funding from the European Union's Horizon Europe Research and Innovation Programme under grant agreement no. 2031928—"Highly Energy-Efficient Resistive Switching in Defect- and Strain- Engineered Mott Insulators for Neuromorphic Computing Applications". Views and opinions expressed are; however, those of the authors only and do not necessarily reflect those of the European Union or the European research council. The work at UCSD was supported by the U.S. Air Force Office of Scientific Research under Award no. FA9550-20-1-0242. D.D. and Y.K. would like to thank Dr. Richard Tran for insightful discussions concerning DFT simulations. J.d.V. acknowledges support from the Spanish Ministry of Science through a Ramón y Cajal Fellowship (RYC2021-030952-I).

Conflict of Interest

The authors declare no conflict of interest.

Data Availability Statement

The data used in this publication can be accessed in the following link: https://zenodo.org/record/7908912#.ZGXkpnZBxPY

Keywords

metal-insulator transitions, Mott insulator, neuromorphic computations, resistive switching, strain engineering

Received: October 12, 2022
Revised: April 4, 2023
Published online: May 19, 2023

[1] M. Imada, A. Fujimori, Y. Tokura, *Rev. Mod. Phys.* **1998**, *70*, 1039.
[2] D. B. McWhan, A. Menth, J. P. Remeika, W. F. Brinkman, T. M. Rice, *Phys. Rev. B* **1973**, *7*, 1920.
[3] A. Georges, G. Kotliar, W. Krauth, M. J. Rozenberg, *Rev. Mod. Phys.* **1996**, *68*, 13.
[4] H. Kuwamoto, J. M. Honig, J. Appel, *Phys. Rev. B* **1980**, *22*, 2626.
[5] F. Rodolakis, J.-P. Rueff, M. Sikora, I. Alliot, J.-P. Itié, F. Baudelet, S. Ravy, P. Wzietek, P. Hansmann, A. Toschi, M. W. Haverkort, G. Sangiovanni, K. Held, P. Metcalf, M. Marsi, *Phys. Rev. B* **2011**, *84*, 245113.
[6] F. Rodolakis, P. Hansmann, J.-P. Rueff, A. Toschi, M. W. Haverkort, G. Sangiovanni, A. Tanaka, T. Saha-Dasgupta, O. K. Andersen, K. Held, M. Sikora, I. Alliot, J.-P. Itié, F. Baudelet, P. Wzietek, P. Metcalf, M. Marsi, *Phys. Rev. Lett.* **2010**, *104*, 47401.
[7] D. Grieger, F. Lechermann, *Phys. Rev. B* **2014**, *90*, 115115.
[8] F. Lechermann, N. Bernstein, I. I. Mazin, R. Valentí, *Phys. Rev. Lett.* **2018**, *121*, 106401.
[9] H. T. Zhang, P. Panda, J. Lin, Y. Kalcheim, K. Wang, J. W. Freeland, D. D. Fong, S. Priya, I. K. Schuller, S. K. R. S. Sankaranarayanan, K. Roy, S. Ramanathan, *Appl. Phys. Rev.* **2020**, *7*, 011309.
[10] J. del Valle, J. G. Ramírez, M. J. Rozenberg, I. K. Schuller, *J. Appl. Phys.* **2018**, *124*, 211101.
[11] C. Adda, M.-H. Lee, Y. Kalcheim, P. Salev, R. Rocco, N. M. Vargas, N. Ghazikhanian, C.-P. Li, G. Albright, M. Rozenberg, I. K. Schuller, *Phys. Rev. X* **2022**, *12*, 11025.
[12] P. A. Metcalf, S. Guha, L. P. Gonzalez, J. O. Barnes, E. B. Slamovich, J. M. Honig, *Thin Solid Films* **2007**, *515*, 3421.
[13] C. Adda, L. Cario, J. Tranchant, E. Janod, M.-P. Besland, M. Rozenberg, P. Stoliar, B. Corraze, *MRS Commun.* **2018**, *8*, 835.
[14] P. Homm, M. Menghini, J. W. Seo, S. Peters, J.-P. Locquet, *APL Mater.* **2021**, *9*, 21116.
[15] M. Querré, E. Janod, L. Cario, J. Tranchant, B. Corraze, V. Bouquet, S. Deputier, S. Cordier, M. Guilloux-Viry, M.-P. Besland, *Thin Solid Films* **2016**, *617*, 56.

[16] N. Alyabyeva, J. Sakai, M. Bavencoffe, J. Wolfman, P. Limelette, H. Funakubo, A. Ruyter, *Appl. Phys. Lett.* **2018**, *113*, 241603.
[17] P. Salev, J. del Valle, Y. Kalcheim, I. K. Schuller, *Proc. Natl. Acad. Sci. USA* **2019**, *116*, 8798.
[18] Y. Kalcheim, C. Adda, P. Salev, M.-H. Lee, N. Ghazikhanian, N. M. Vargas, J. del Valle, I. K. Schuller, *Adv. Funct. Mater.* **2020**, 2005939.
[19] Y. Kalcheim, N. Butakov, N. M. Vargas, M.-H. Lee, J. del Valle, J. Trastoy, P. Salev, J. Schuller, I. K. Schuller, *Phys. Rev. Lett.* **2019**, *122*, 57601.
[20] E. B. Thorsteinsson, S. Shayestehaminzadeh, U. B. Arnalds, *Appl. Phys. Lett.* **2018**, *112*, 161902.
[21] J. Brockman, M. G. Samant, K. P. Roche, S. S. P. Parkin, *Appl. Phys. Lett.* **2012**, *101*, 051606.
[22] G. D. Zhang, L. Hu, M. Zhu, R. H. Wei, R. R. Zhang, W. H. Song, X. B. Zhu, Y. P. Sun, *Phys. Rev. B* **2022**, *105*, 35140.
[23] H. Schuler, S. Klimm, G. Weissmann, C. Renner, S. Horn, *Thin Solid Films* **1997**, *299*, 119.
[24] D. Wickramaratne, N. Bernstein, I. I. Mazin, *Phys. Rev. B* **2019**, *100*, 205204.
[25] J. Trastoy, Y. Kalcheim, J. del Valle, I. Valmianski, I. K. Schuller, *J. Mater. Sci.* **2018**, *53*, 9131.
[26] I. Valmianski, J. G. Ramirez, C. Urban, X. Batlle, I. K. Schuller, *Phys. Rev. B* **2017**, *95*, 155132.
[27] H. Hajihoseini, E. B. Thorsteinsson, V. v Sigurjonsdottir, U. B. Arnalds, *Appl. Phys. Lett.* **2021**, *118*, 161602.
[28] L. Dillemans, T. Smets, R. R. Lieten, M. Menghini, C.-Y. Su, J.-P. Locquet, *Appl. Phys. Lett.* **2014**, *104*, 071902.
[29] B. S. Allimi, S. P. Alpay, D. Goberman, T. Huang, J. I. Budnick, D. M. Pease, A. I. Frenkel, *J. Mater. Res.* **2007**, *22*, 2825.
[30] E. R. Dobrovinskaya, L. A. Lytvynov, V. Pishchik, *Sapphire: Material, Manufacturing, Applications*, (Eds.: V. Pishchik, L. A. Lytvynov, E. R. Dobrovinskaya), Springer US, Boston, MA, **2009**, pp. 55–176.
[31] L. J. Eckert, R. C. Bradt, *J. Appl. Phys.* **1973**, *44*, 3470.
[32] J. Sakai, P. Limelette, H. Funakubo, *Appl. Phys. Lett.* **2015**, *107*, 241901.
[33] J. Brockman, N. P. Aetukuri, T. Topuria, M. G. Samant, K. P. Roche, S. S. P. Parkin, *Appl. Phys. Lett.* **2011**, *98*, 152105.
[34] J. Kim, C. Ko, A. Frenzel, S. Ramanathan, J. E. Hoffman, *Appl. Phys. Lett.* **2010**, *96*, 213106.
[35] H. Kim, T. v Slusar, D. Wulferding, I. Yang, J.-C. Cho, M. Lee, H. C. Choi, Y. H. Jeong, H.-T. Kim, J. Kim, *Appl. Phys. Lett.* **2016**, *109*, 233104.
[36] Q. Guo, B. Noheda, *npj Quantum Mater.* **2021**, *6*, 72.
[37] L. Puntigam, M. Altthaler, S. Ghara, L. Prodan, V. Tsurkan, S. Krohns, I. Kézsmárki, D. M. Evans, *Adv. Electron. Mater.* **2022**, *8*, 2200366.
[38] W. R. Robinson, *Mater. Res. Bull.* **1974**, *9*, 1091.
[39] D. Wickramaratne, N. Bernstein, I. I. Mazin, *Phys. Rev. B* **2019**, *99*, 214103.
[40] J. C. Leiner, H. O. Jeschke, R. Valentí, S. Zhang, A. T. Savici, J. Y. Y. Lin, M. B. Stone, M. D. Lumsden, J. Hong, O. Delaire, W. Bao, C. L. Broholm, *Phys. Rev. X* **2019**, *9*, 11035.